ORIGINAL PAPER

Gold nanorod separation and characterization by asymmetric-flow field flow fractionation with UV–Vis detection

Julien Gigault · Tae Joon Cho · Robert I. MacCuspie · Vincent A. Hackley

Abstract The application of asymmetric-flow field flow fractionation (A4F) for low aspect ratio gold nanorod (GNR) fractionation and characterization was comprehensively investigated. We report on two novel aspects of this application. The first addresses the analytical challenge involved in the fractionation of positively charged nanoparticles by A4F, due to the interaction that exists between the negatively charged native membrane and the analyte. We show that the mobile phase composition is a critical parameter for controlling fractionation and mitigating the membrane-analyte interaction. A mixture of ammonium nitrate and cetyl trimethyl ammonium bromide at different molar ratios enables separation of GNRs with high recovery. The second aspect is the demonstration of shape-based separation of GNRs in A4F normal mode elution (i.e., Brownian mode). We show that the elution of GNRs is due both to aspect ratio and a steric-entropic contribution for GNRs with the same diameter. This latter effect can be explained by their orientation vector inside the A4F channel. Our experimental results demonstrate the relevance of the theory described by Beckett and Giddings for non-spherical fractionation (Beckett and Giddings, *J Colloid and Interface Sci* 186(1):53–59, 1997). However, it is shown that this theory has its limit in the case of complex GNR mixtures, and that shape (i.e., aspect ratio) is the principal material parameter controlling elution of GNRs in A4F; the apparent translational diffusion coefficient of GNRs increases with aspect ratio. Finally, the performance of the methodology developed in this work is evaluated by the fractionation and characterization of individual components from a mixture of GNR aspect ratios.

Keywords Field flow fractionation · Gold · Nanoparticle · Nanorod · Shape separation · Hyphenated technique · Elution mechanism · Positive charge

Introduction

Metallic nanorods have attracted increasing attention due to the ease of preparation, the large number of synthetic methods available, the high uniformity achievable, and control over the aspect ratio, which in turn is primarily responsible for controlling the optical properties [2, 3]. Gold is widely recognized as the most important noble metal nanomaterial due to its unique optical response and its potential use in catalytic, biosensing, nanomedicine and electronic applications [2, 4–9]. The development of well-controlled shapes and novel structures of gold nanoparticles has therefore developed into an emerging research topic in its own right. More specifically, gold nanorods (GNRs) have many fascinating properties and have been used in sensors, for information storage, and in a number of biomedical applications such as photothermal therapy [10–15].

While substantial research has been carried out to develop and utilize single GNRs and GNR ensembles as sensors, many important unexplored aspects and challenges remain before GNRs can be effectively used in practice. One of these challenges is the need to achieve sensitive and relevant in situ characterization of GNR shape and size distributions. It is in this context that advanced separation techniques coupled to multiple detection modalities can play a significant role. Chromatographic techniques, such as size

J. Gigault · T. J. Cho · R. I. MacCuspie · V. A. Hackley (✉)
Materials Measurement Science Division, National Institute of Standards and Technology,
100 Bureau Drive, Stop 8520,
Gaithersburg, MD 20899-8520, USA
e-mail: vince.hackley@nist.gov

exclusion chromatography (SEC), have been successfully utilized to separate GNR mixtures [16]. However, SEC is limited by low resolution and selectivity (based on size and shape) and also a poor recovery resulting from irreversible adsorption of GNRs onto the column packing material, even when surfactants are used in the mobile phase [16].

Recently asymmetric-flow field flow fractionation (A4F), a hydrodynamic chromatographic separation technique, has emerged as a high performance alternative capable of characterizing both spheroidal and high aspect ratio nano-objects [17–26]. Reports indicate that A4F is a promising technique due to its versatility, dynamic range and size-resolution potential. Additional advantages of A4F include the ability to couple with multiple detectors that provide complementary results on the size and shape of the analytes, and the potential for high recovery due to the absence of a stationary phase. Detectors typically used in conjunction with A4F include multi-angle light scattering (MALS) and quasi-elastic light scattering (QELS), which provide size-related information on the analytes (i.e., radius of gyration, R_g, hydrodynamic radius, R_h, and translational diffusion coefficient, D). Also the shape- and size-dependent optical properties can be conveniently obtained by coupling with a diode array detector (DAD) that provides real-time UV–vis absorption spectra. Indeed UV–vis is a very useful tool for the characterization of optically active gold nano-objects, due to their characteristic surface plasmon resonance (SPR) bands. GNRs have two characteristic SPR bands, one due to the transverse oscillation of the electrons that appears around 520 nm and the other due to the longitudinal plasmon resonance appearing at longer wavelengths [27–30]. The transverse SPR band, which does not depend on the aspect ratio, occurs at the same or similar wavelength as the SPR for spheres of equivalent diameter [28]. In contrast, the wavelength of the longitudinal SPR band increases with increasing aspect ratio [31].

Despite the promising capabilities of A4F for fractionation and characterization of GNRs, the development and optimization of methodology remains largely unexplored. Herein, we report the results of a comprehensive investigation in which GNRs of relatively low aspect ratios (i.e., < 10) have been successfully fractionated based on their aspect ratio and simultaneously characterized both dimensionally and optically. We address major practical challenges for application of A4F to GNRs, such as the adverse effect of attractive GNR-membrane interactions; commercially available membranes for A4F generally carry a negative charge in aqueous media, and therefore only negatively charged or neutral nano-objects can be easily fractionated by A4F using an unmodified membrane. GNRs are typically positively charged as a result of a widely used synthesis route that depends on adsorption of cationic surfactants; hence, the analyte is absorbed onto the membrane surface resulting in

elution failure. The second challenge involves the morphological complexity characterized by the variation in aspect ratio. Consequentially, poor resolution for separation and low recovery must be overcome by controlling critical factors including the mobile phase composition, the channel/cross flow ratio, and wavelength limitations of the DAD. Indeed, the innovative aspect of this research is the novel fractionation capacity of A4F demonstrated by the successful separation of GNR components from a complex mixture, not based on size or length, but on the aspect ratio, regardless of the GNR surface charge state.

Experimental

Reagents

Ammonium nitrate (NH_4NO_3, 99 %) and cetyl trimethyl ammonium bromide (CTAB) were purchased from VWR (Bridgeport, NJ)[1] and used without further purification. GNRs in aqueous suspension were obtained from Nanopartz (Loveland, CO). Vendor provided information and material characteristics are summarized in Table 1; while electron microscopy images and UV–vis absorbance spectra for the as received stock solutions are provided in the Electronic Supplementary Material (Electronic Supplementary Material, see Figures S1 and S2, respectively). Deionized (DI) water was generated by an Aqua Solutions (Jasper, GA, USA) ultra-low TOC biological grade water purification system. All A4F mobile phases were passed through a 0.2 μm regenerated cellulose filter from VWR. Stock solutions of ammonium nitrate and CTAB were prepared by dissolving the required amount in DI water (18 MΩ·cm)

Instrumentation and methods

The A4F system used in this study is an Eclipse 3+ (Wyatt Technology, Santa Barbara, CA). A 350 μm thick spacer was used, and channel dimensions were 26.5 cm in length and from (2.1 to 0.6) cm in width. For all experiments, polyethersulfone (PES) membranes with a 10 kDa cut-off were used (Wyatt Technology). Flows (main flow and cross flow) were controlled with an Agilent Technologies (Santa Clara, CA) 1100 series isocratic pump equipped with a degasser (Gastorr TG-14, Flom Co., Ltd., Tokyo, Japan). In this study, considering the size range of GNRs, the main flow (V_p) was fixed at 0.5 mL min^{-1}. Injections were performed by a manual injection valve (Rheodyne 7725i, IDEX Corporation, Oak Harbor, WA) equipped with a 100 μL

Table 1 GNR material properties as reported by the commercial vendor. TSPR refers to the transverse mode plasmon resonance band and LSPR refers to the longitudinal mode

Product ID	Sample name[a]	Length (nm)	Diameter (nm)	Aspect ratio	pH	Zeta potential (mV)	TSPR peak (nm)	TSPR AU[b]	LSPR peak (nm)	LSPR AU[b]	Concentration (mg mL^{-1})
30-25-550	GNR1.4	34	25	1.4	3.2	+38.2	550	1.2	524	0.75	0.043
30-25-700	GNR3.1	77	25	3.1	3	+39	712	1.2	521	0.2	0.060
30-10-780	GNR3.8	38	10	3.8	4	+40	782	1	512	0.3	0.040
30-10-850	GNR4.4	44	10	4.4	4.2	+38	844	1.2	509	0.16	0.040

[a] Number is the reported aspect ratio of corresponding GNR

[b] Absorbance units (i.e., log I_0/I measured in a 1 cm pathlength cell)

stainless steel sample loop . The detection train consisted of a 1200 series UV–Vis absorbance DAD (Agilent Technologies) with a spectral range from (190 to 950) nm and a sampling rate of 20 Hz; a fiber optic based MALS detector (DAWN HELI-OS, Wyatt Technology); a fiber optic based QELS detector at a scattering angle of 90° (DynaPro, Wyatt Technology). Data from the different detectors was collected and analyzed using Astra version 5.3.1.18 software (Wyatt Technology).

All measurements were conducted at (20±0.1) ºC, but temperature was directly controlled only in the light scattering cell. Eluting samples were subject to ambient temperatures outside of this cell, where the ambient temperature was generally within 2ºC of the experimental temperature. A 100 µL injection of bulk solution was performed for each sample. Discrete measurement results are reported as the mean with an associated uncertainty of one standard deviation (presented as an interval or error bar) based on typically 3 to 5 replicates performed under repeatability conditions. A4F traces represent the mean of 3 to 5 replicate injections, where the average coefficient of variation between replicate elutions is far less than 1 %.

Practical parameters of A4F theory

Two modes of elution are possible in A4F: *viz.* normal (or Brownian) and steric. The dominant mode is determined by the fractionation conditions (channel thickness and mobile phase) and the analyte size range. Considering the size range involved in the present study, the normal mode should be operative. The elution time in A4F normal mode is determined by the diffusion coefficient (**D**) of the analyte (and through **D** by the hydrodynamic radius **R_h**, according to the well known Stokes-Einstein relationship) as shown in Eq. (1) [32]:

$$D = \frac{V_c \cdot \omega^2 \cdot R}{6 \cdot V_0 \cdot (1 - R)^{\frac{1}{3}}} \tag{1}$$

Here, V_0 is void volume (m^3) - determined experimentally by tracing unretained dissolved species, V_c is cross flow rate (m^3 s^{-1}), η is viscosity of the mobile phase (kg m^{-1} s^{-1}), R is retention ratio defined as t_0/t_R (ratio between void time and retention time), ω is channel thickness (m). When V_c is kept constant and retention time (t_R) is sufficiently long (i.e., $0.03 < R < 0.1$), then Eq. (1) can be simplified to Eq. (2), yielding a simple linear relationship between D and R:

$$D = \frac{V_c \cdot \omega^2 \cdot R}{6 \cdot V_0} \tag{2}$$

Here, the retention ratio R is an appropriate parameter to judge the efficiency of the fractionation process. Generally, R should be in the range from 0.025 to 0.1 [32]. With R over 0.1 the approximation described by Eq. (2) cannot be applied, and with R below 0.025 the resolution decreases because of excessive sample zone broadening. This signal broadening is observed by an increase in the elution time range associated with a peak signal.

The recovery ($R\%$), i.e., the ratio between recovered mass after analysis and injected mass, is expressed as:

$$R\% = \frac{S}{S_0} \cdot 100 \tag{3}$$

Here, S and S_0 are the surface area under the peak signal with and without applying cross-flow, respectively. $R\%$ permits the evaluation of the performance ability of the A4F system to fractionate analytes without significant loss of analyte or analytical information.

Results and discussion

Influence of the mobile phase composition

In the case of GNRs, and other positively charged nano-objects, a major challenge for A4F fractionation arises from

the fact that the membrane or accumulation wall (which provides cross flow) is typically negatively charged, and thus irreversible attachments can occur resulting in a noisy peak with low recovery, as is demonstrated in the Electronic Supplementary Material (see Figure S3). A convenient and adaptable method to resolve this issue is to optimize the mobile phase; another option is to chemically modify the membrane. Here we have chosen the former method, due to its simplicity and questions concerning the stability and homogeneity of chemically functionalized membranes. The mobile phase composition and ionic strength are the most important parameters for controlling or mitigating the interaction-repulsion of the analytes at the native membrane surface.

In general, the mobile phase in A4F should provide the same electrical polarity between analytes and the membrane surface. In order to control the elution of GNRs by controlling the interaction-repulsion with the membrane, it was proposed to add an inert salt (NH_4NO_3) and to combine the salt with the cationic surfactant CTAB at different molarity percentages while maintaining the total mobile phase ionic strength constant at 0.5 $mmol\,L^{-1}$ (as it was previously found optimal for gold nanoparticle fractionation—see Figure S3 in the Electronic Supplementary Material) [19]. The use of a simple salt in the A4F mobile phase allows screening of electrostatic repulsion between nanoparticles and the negatively charged membrane [19], where a balance is sought between overly repulsive interactions (leading to no retention, resulting in no fractionation) and no repulsion (resulting in poor recovery and the band broadening effect).

Our preliminary results indicated that CTAB was required in the mobile phase to provide some repulsive force between the membrane and GNRs (see section Results and Discussion in SI for further details), which are otherwise mutually attractive. However, we found that using CTAB alone resulted in too much repulsion between GNRs and the membrane, and therefore the analytes were unretained on the membrane and pre-eluted without sufficient fractionation. Hence, the challenge in this case was to find an appropriate ratio between NH_4NO_3 and CTAB to afford an acceptable fractionation of GNRs without significant loss of material. For mobile phase optimization, several NH_4NO_3/CTAB ratios were tested, and Table 2 summarizes the R% and R values obtained for the different GNRs in mobile phases prepared as a function of composition ratio. To reveal the best compromise between R% and R with minimal instrumental variables, V_p and V_c were kept constant at 0.5 $mL\,min^{-1}$ and 0.8 $mL\,min^{-1}$, respectively. In addition, associated fractograms for the different GNRs with the different mobile phase compositions summarized in Table 2 are presented in Fig. 1.

At low CTAB content (5 % of the total ionic strength, i.e. 0.025 $mmol\,L^{-1}$), an improvement of the signal was observed for GNR1.4 and GNR3.1 compared to the signals obtained with only 0.5 $mmol\,L^{-1}$ of NH_4NO_3 (see Electronic Supplementary Material, Figure S3). Nevertheless, the recovery obtained was unacceptably low, especially for GNR3.8 and GNR4.4. These low recoveries are due to attractive interactions between GNRs and the accumulation wall membrane. The corresponding fractograms for these two GNRs confirmed the strong interactions based on the noisy and broadened signals (Fig. 1a). The CTAB quantity in this mobile phase system is too low to create sufficient repulsion between GNRs and the membrane (negatively charged surface). By increasing the proportion of CTAB in the mobile phase, it appears that the recovery reaches a maximum for all GNR samples at a ratio 30 %:70 % (CTAB:NH_4NO_3) while simultaneously the retention ratio increases. Clearly, this retention ratio increase is due to the increasing repulsion between GNRs and the membrane afforded by the increasing load of CTAB associated with the membrane surface. On the other hand, when the concentration of CTAB is over 0.25 $mmol\,L^{-1}$, a decrease in recovery appears due to the loss of materials through pre-elution (note this is not due to membrane attachment), and this effect is promoted by excessive repulsive interactions due to high CTAB concentration (see Section 3 in the Electronic Supplementary Material, Figures S4 and S5). This puts an upper limit on the concentration with respect to recovery.

A4F fractograms for all GNR samples with mobile phase composition ratio of 70 %:30 % (CTAB:NH_4NO_3) are characterized by three distinguishable peaks (Fig. 1d), which indicates the complexity of GNR-membrane interactions at higher CTAB concentrations and suggests the formation of secondary structures. The first relatively small peak localized at the void time can be explained by strong repulsion between analytes and the membrane surface leading to a pre-elution of partially unretained GNRs, as previously observed by using CTAB exclusively in the mobile phase and explained further in the Electronic Supplementary Material (see Figure S4). The other characteristic signals that appear at retarded retention times show a signal splitting pattern most likely associated with the major peak of retained analyte. It is not yet fully clear, but presumably these splitting signals (even for monodisperse samples) might be due to a very sensitive response by A4F, either to the degree of interaction that occurs inside the channel between analyte and the accumulation wall or to the slight differences of sample components that possibly result from the manufacturing process.

From the results presented thus far, it appears that the best compromise is obtained for the CL2 mobile phase, containing 30 % CTAB and 70 % of NH_4NO_3. This mobile phase composition allows the highest recovery values (R%) and a reasonable retention ratio (R) ranging from 0.035 to

Table 2 Recovery and retention ratio obtained for the four GNRs with a selection of mobile phase compositions tested at an ionic strength of 0.5 mmol L^{-1} and channel (V_p)/cross flow (V_c) ratio fixed at 0.5/0.8. Results are reported as the mean from 5 replicate analyses; the average standard deviation for the recovery and the retention ratio was 0.5 % and 0.3 %, respectively. The values determined from the A4F traces represent the mean of 3 to 5 replicate injections, where the average coefficient of variation between replicate elutions (not shown) is less than 1 %
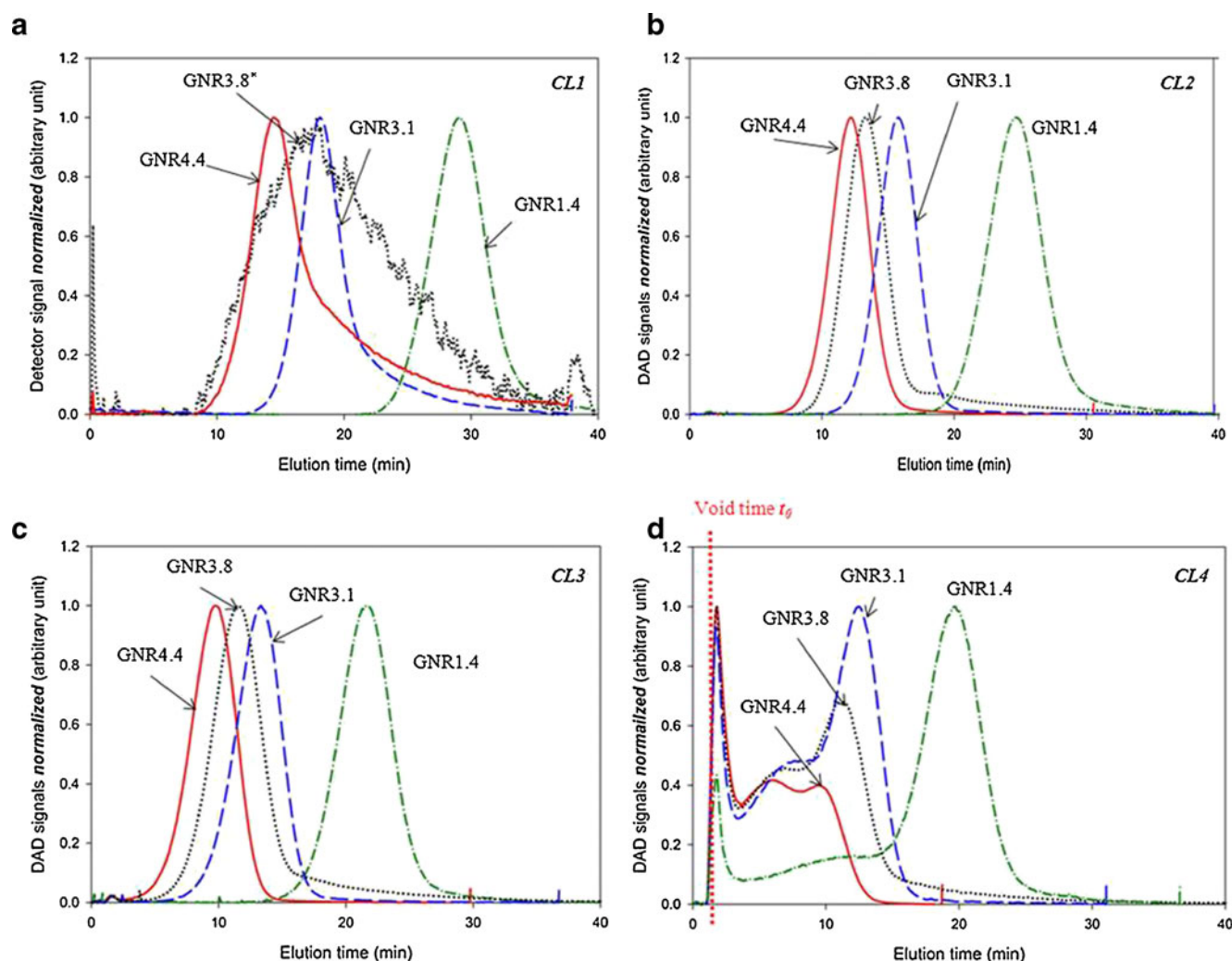
	Fixed molarity ratio CTAB : NH$_4$NO$_3$									
	5 % : 95 % (CL1)		30 % : 70 % (CL2)		50 % : 50 % (CL3)		70 % : 30 % (CL4)		100 % : 0 % (CL5)	
	R%	R	R%	R	R%	R	R%	R	R%	R
GNR1.4	81.5	0.052	101.5	0.056	72.37	0.069	57.4	0.076	38.8	0.084
GNR3.1	73.2	0.080	108.9	0.095	99.6	0.113	30.5	0.120	24.2	0.129
GNR3.8	7	0.086	87.7	0.112	79.3	0.130	37.3	0.133	22.5	0.139
GNR4.4	19.1	0.109	101.7	0.123	99.7	0.154	30.1	0.159	18.2	0.167

Fig. 1 Typical DAD-based fractograms tuned at the appropriate TSPR wavelength position (550 nm, 710 nm, 780 nm and 850 nm) for the four different GNR samples (GNR1.4, GNR3.1; GNR3.8; and GNR4.4 respectively) realized with the same fractionation condition (10 kDa PES membrane, 350 μm spacer thickness, V_p/V_c=0.5/0.8 mL min^{-1}) as a function of the NH$_4$NO$_3$/CTAB ratio (see Table 1) at a constant ionic strength of 0.5 mmol L^{-1} in the mobile phase: **a** CL1; **b** CL2; **c** CL3; **d** CL4. (*):low signal amplified and normalized in order to compare with other fractograms. The *red*, *black*, *blue* and *green lines* correspond to *GNR4.4*, *GNR3.8*, *GNR3.1* and *GNR1.4*, respectively

0.13. Additionally, the R values obtained with this mobile phase result in a Brownian (or normal) mode elution in A4F.

Elution mechanism

Next, we evaluated the effect of the flow ratio on the retention behavior of GNR dispersions and their separation in the A4F channel. The influence of the applied V_c was investigated by examining the retention ratio, recovery, and the signal broadening characterized by peak width and height. As it was explained above (see Instrumention and Methods), V_p was fixed at 0.5 mL min^{-1} for the experiments and provided a good compromise between elution time and unacceptably high flow pressures, which indicates V_p is not the crucial parameter for fractionation in this case.

In this research, V_c was investigated over a range from (0.5 to 3.0) mL min^{-1}, but only a V_c range from (0.8 to 2.3) mL min^{-1} yielded an R value from 0.03 to 0.1, which is critical for normal mode elution. Notably, the recovery for all GNR samples obtained by this study of flow ratios revealed values equally high to those obtained with fixed V_c (i.e., 0.8 mL min^{-1}) described above. This means that the optimized mobile phase system (CL2) is sufficiently robust for the characterization of GNRs regardless of the cross-flow rate chosen. In terms of peak broadening, Fig. 2 presents the variation of the DAD-based peak height at the corresponding TSPR position and width (δt_R) for each tested GNR as a function of the applied V_c. Results show that even if no change in recovery is observed, a peak broadening effect appears above $V_c \approx 1.8$ mL min^{-1}. Above this value the peak width increases for all GNR samples, but particularly for GNR1.4. In other words, the peak broadening is inversely

proportional to the aspect ratio, and this can be attributed to the lower retention ratio characteristic of the higher residence time in the channel yielding an excessive sample zone broadening.

With respect to the retention ratio obtained for different V_c, Fig. 3 presents the variation of R for the GNRs as a function of $1/V_c$; a linear relationship between R and $1/V_c$ is clearly apparent. According to Eq. (2), this linear relationship confirms the normal mode elution of GNRs, indicating the slope is directly proportional to the translational diffusion coefficient of the analytes under conditions where the spacer thickness is held constant and the void time is a determined quantity.

The diffusion coefficient for each GNR was determined by A4F measurement and the results are summarized in Table 3 (columns 1 and 2). The values obtained by a mathematical model are also described in Table 3 for comparison (columns 3 and 4). The mathematical model allows one to determine the diffusion coefficient for Brownian rods based on their size parameters (length L, diameter d, and aspect ratio L/d), and is expressed in Eq. 4 [33, 34]:

$$D = \frac{kT}{3\pi\eta L}\left[\ln\left(\frac{L}{d}\right) + 0.312 + 0.565\frac{d}{L} + 0.100\left(\frac{d}{L}\right)^2\right] \quad (4)$$

Table 3 shows a general lack of consistency between the measured and calculated values when the FFF model for spherical particles is compared with the Brownian calculations; only in the case of GNR1.4, which is closest to spherical, do results agree statistically. In order to explain these differences, a theoretical study by Beckett and Giddings [1] can be used to rationalize the discrepancies. Indeed, these authors extended the general retention equation for FFF
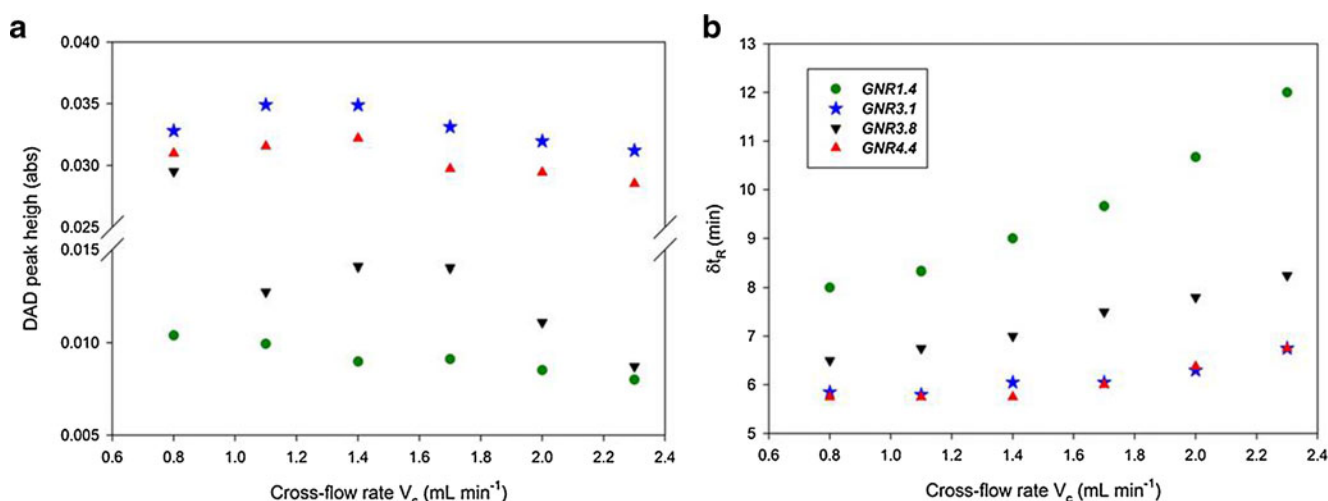

Fig. 2 Variation of the DAD peaks **a** height and **b** width for the GNR samples according to the cross-flow rate (the standard deviations for peak height and width are not shown, because they are smaller than the symbol size, i.e., of order 0.4 %)
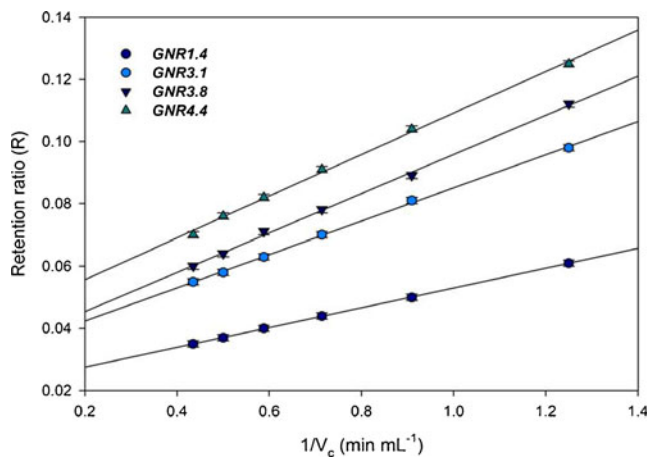
Fig. 3 Variation of the retention ratio for GNR samples as a function of the inverse cross-flow rate

normal mode elution to include a steric perturbation due to entropy associated with the orientation of non-spherical particles. In this typical mode of elution, perturbed by the steric-entropic contribution of the rod-like shape, Eq. (2) can be rewritten as [1]:

$$D = \frac{V_c \cdot \omega^2 \cdot R}{12 \cdot V_0} \tag{5}$$

In this case the "corrected" diffusion coefficient (labeled "non-spherical" in Table 3, column 2) is generally closer to those values obtained by the Brownian model. Nevertheless there remains a difference between corrected and calculated D, which may be explained by the low aspect ratio in the present study. In the literature [34], it has been shown by DLS characterization of GNRs that a significant deviation occurs between measured and calculated D for low aspect ratios (≤ 8). These deviations could be attributed to the effect of the capping agent on the diffusion coefficient, because it contributes to the hydrodynamic radius. To test this, we applied the Brownian model using a reasonable approximation for the CTAB coating thickness (6.5 ± 0.2 nm). Results indicate that the difference between non-spherical FFF measurement results and the Brownian model decreases with the inclusion of the CTAB coating (the

exception being GNR3.1). This result suggests that the contribution of the CTAB coating is important, especially for low GNR aspect ratios. The residual deviation between D values (i.e., between the FFF results and the Brownian model), suggests that the separation is not only due to the diffusion coefficient, but that the aspect ratio, through its steric-entropic effect, also has an influence on the A4F separation process. Indeed, D determined by the Brownian model should depend on the length of the rod; however, D obtained by A4F measurements in this study are proportional to the GNR aspect ratio, and also R varies linearly with the corresponding aspect ratio (Fig. 4), without any clear relationship to rod length (Table 1).

Moreover, the separation process based on D and the aspect ratio in this investigation does not fully explain why longer GNRs with the same diameter (i.e., GNR1.4 and GNR3.1 for diameter of 25 nm, and GNR3.8 and GNR4.4 for diameter of 10 nm) elute earlier than the shorter GNRs. These observations are inconsistent with previously reported results for flexible nanorods and nanotubes with high aspect ratio (≥ 100), [18, 35, 36] where shorter lengths generally elute first.

Adapted from the Beckett and Giddings theoretical framework for non-spherical particle elution, nanorods in the A4F channel, due to their steric-entropic contribution, can be assimilated to a unit sphere corresponding to the nanorod orientation vector (unit of length), which depends on the rod length and the distance from the accumulation wall. So, the concentration profile of the analyte in the sample for rod-like particles can be expressed as: [1]

$$c(x) = c_0 e^{-\frac{x}{l}} \left(2\frac{x}{L}\right) \tag{6}$$

The term, $c(x)/c_0$ is the relative concentration of the analyte in the A4F channel, l is the mean layer thickness, x is the distance between the analyte and accumulation wall, and L is the rod length. Eq. (6) means that for rods with the same diameter, the longer rods have a concentration profile further removed from the accumulation wall compared to the shorter rods, and consequently elution is faster for longer rods independent of V_c. According to the parabolic velocity

Table 3 GNR diffusion coefficients, D ($\times 10^{-11}\,\mathrm{m^2\,s^{-1}}$), determined by A4F and calculated according to Eq. (4)

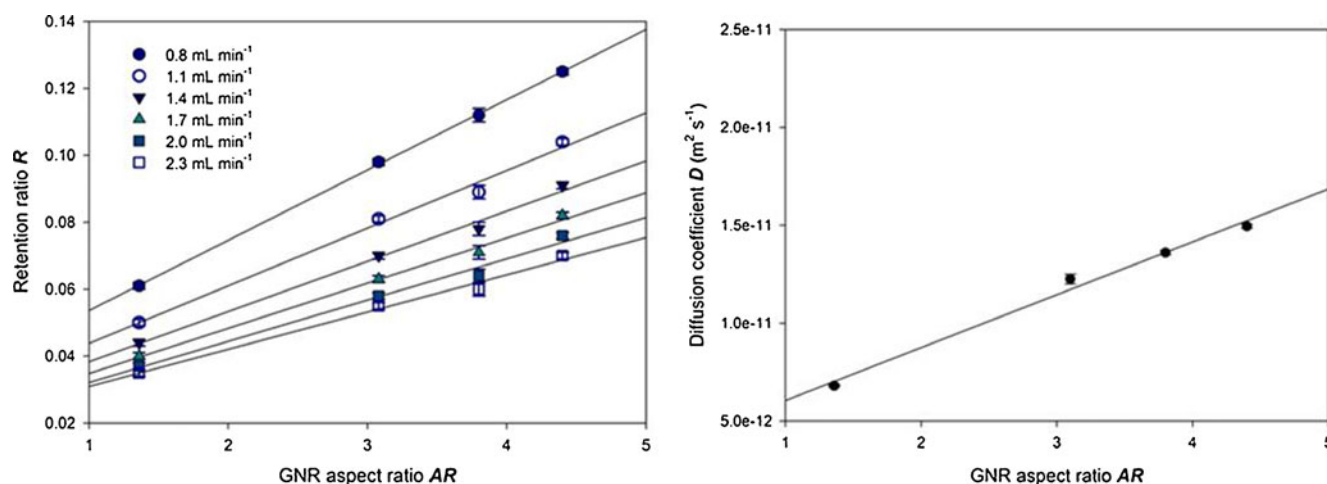| Sample	A4F measurement results FFF model		Calculated results Brownian model	
	Spherical [32]	Non-spherical [1]	Hard core size	With 6.5 ± 0.2 nm CTAB coating
GNR1.4	1.36 ± 0.01	0.68 ± 0.01	1.37	0.58 ± 0.10
GNR3.1	2.45 ± 0.05	1.23 ± 0.03	0.91	0.77 ± 0.12
GNR3.8	2.72 ± 0.02	1.36 ± 0.01	1.98	1.41 ± 0.15
GNR4.4	2.99 ± 0.02	1.50 ± 0.01	1.88	1.34 ± 0.17

Fig. 4 Representation of **a** variation of GNR retention ratio as a function of the aspect ratio, and the **b** variation of GNR diffusion coefficient determined by A4F also as a function of aspect ratio

profile of the channel flow, particles located higher in the channel elute faster than those closer to the membrane surface. This explains why, in the case of GNRs with the same diameter but different lengths, the longer GNRs elute first.

Nevertheless this theory does not explain why, in the case of GNR3.1 and GNR3.8, with different diameters, the shorter length rods (GNR3.8, length of 38 nm) elute earlier than the longer rods (GNR3.1, length of 77 nm). In this particular case the theory from Beckett and Giddings is not consistent with the results; however, it is possible to explain this phenomenon based on the GNR aspect ratio without needing to consider separately the diameter and/or the length. As the elution occurs in normal mode (i.e., a linear relationship exists between R and D), in the small aspect ratio and nanoscale size range, the aspect ratio is the dominant parameter that controls elution of GNRs without needing to consider separately the diameter and/or the length. The theory for the elution of non-spherical particles works best for particles with the same diameter and the same distance from the accumulation wall [1]. The A4F results reported here suggest that the elution of GNRs depend on:

1) GNR aspect ratio, with a linear relationship that is insensitive to the cross-flow,
2) GNR steric-entropy contribution associated with their orientation (for the same diameter but different length).

As mentioned above, the experimental results in this study reveal different but interesting phenomena beyond the classical hard-sphere theory. More specifically, that the retention of asymmetric, but low aspect ratio, nanoparticles (in this case GNRs), under a particular experimental condition, depend directly on the diffusion coefficient and correlated particle shape (aspect ratio), rather than on the rod length alone. Based on the novel concept of separation by

shape instead of size, the capability of A4F was tested not only for characterization of GNRs, but also for separation of individual GNRs from a mixture. Furthermore, the high sensitivity of retention to the relatively small aspect ratio of GNRs (less than 5) used in this study suggests the potential for exploitation of subtle shape-dependent fractionation of nanoparticles, an effect we are exploring for a future publications.

In order to conduct shape-based separation by A4F, the quality of fractionation should be evaluated. Hence, we preliminarily propose to adopt a definition of "selectivity" for shape fractionation derived from classical FFF theory, in which selectivity is defined as *"a measure of the inherent ability of a technique to separate two components"* [32]. In a manner consistent with the basis for classical selectivity determination in A4F (i.e., t_R and hydrodynamic diameter), we propose to define shape characterization selectivity (S_D)
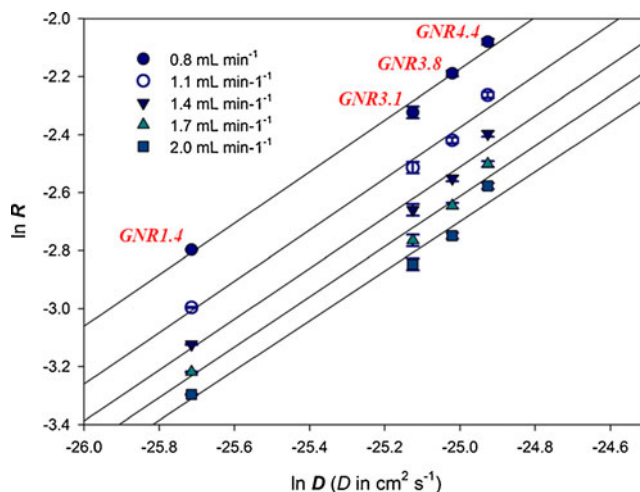

Fig. 5 Representation of ln R versus ln D for GNRs over the range of V_c tested in this study

as a function of D (as it has been demonstrated that GNR diffusivity is linearly proportional to the aspect ratio) and R, such that: [32]

$$S_D = \left| \frac{d\ln R}{d\ln D} \right| \qquad (7)$$

In A4F, separation depends on the diffusion coefficient of the analytes, so that the highest S_D that can be obtained is close to unity [32]. As illustrated in Fig. 5, by plotting $\ln R$ versus $\ln D$ at various cross-flow rates, the relationship is linear, and, according to Eq. (7), the slope of this relationship is equal to S_D. For V_c ranging from (0.8 to 2.0) mL min^{-1}, S_D ranges from 0.857 to 0.888, respectively. These S_D values are close to unity and confirm the efficiency of the method for separating GNRs according to their shape. Indeed, as it was explained previously, the selectivity describes the ability of the technique to fractionate one sample without consideration of its polydispersity and complexity. So a convenient V_c range should be chosen that enables an acceptable selectivity, then an appropriate V_c must be selected for the particular mixture to be investigated, such that the highest possible resolution and recovery are attained.

Validation and applicability

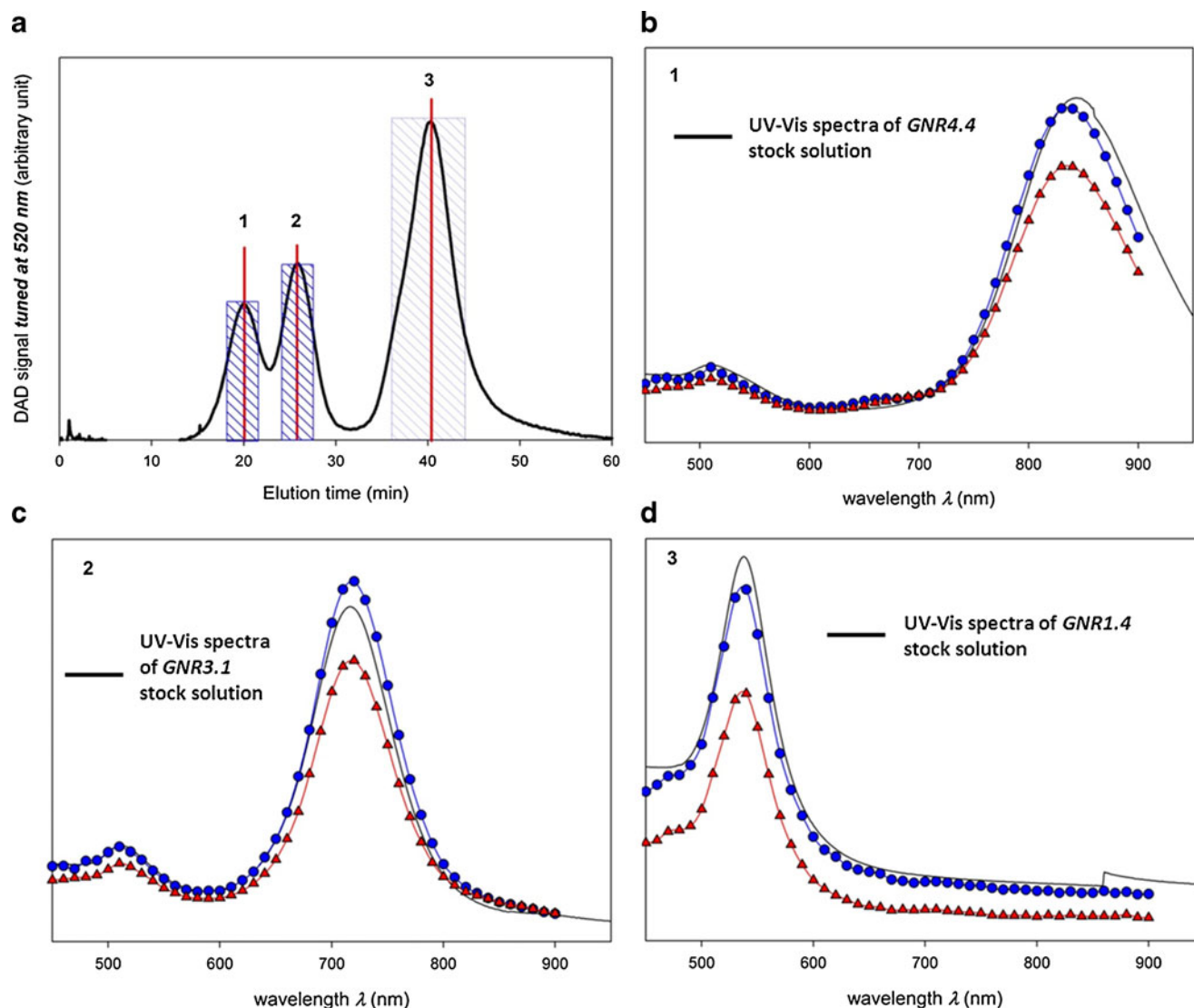We evaluated the efficiency of the method developed in this investigation for separation and characterization of GNR

Fig. 6 a Typical fractograms obtained at the optimal fractionation condition (10 kDa PES membrane, 350 μm spacer thickness, V_c=2.0 mL min^{-1}, V_p=0.5 mL min^{-1} and CL2 mobile phase) for the 3-component GNR mixture (*black line*) with DAD tuned to 520 nm; **b** to **d** the UV–vis spectra measured on-line for GNRs corresponding to the 3 peaks (marked 1,2 and 3 in a) at the top of the signals (*blue line, circles*) and the peak-averaged spectrum (*red line, triangles*), and the UV–vis spectra of the different GNR native suspensions (*black line, no symbols*)

mixtures. A mixture of three GNRs (*GNR1.4*, *GNR3.1* and *GNR4.4*) was prepared by maintaining the same dilution factor. In order to obtain three distinct signals, several elution conditions were tested, and the highest resolution with minimal loss of material to the membrane surface was achieved, with $V_c = 2.0$ mL min^{-1}. The observed fractogram for the mixture, traced using an absorption wavelength of 520 nm, is illustrated in Fig. 6. Additionally, the UV–vis spectrum for each individual peak was measured on-line at two retention times: one spectrum at t_R corresponding at the maximum of the peak and a second spectrum averaged over the whole peak area (average spectrum calculated by the software). These spectra are then compared to the UV–vis spectra obtained for the corresponding individual GNR stock solutions (i.e., unmixed). It appears that all UV–vis spectra correspond correctly and that co-elution of GNRs is not occurring in the mixed system. Furthermore, no difference is observed between the peak-averaged spectrum and the spectrum taken at the top of the peak. Combined, these results confirm that the A4F method can separate individual monodisperse GNRs within a mixture, even where the differences in aspect ratio are relatively small. The UV–vis spectra obtained on-line for the different trace peaks, and compared to the spectra for GNR stock solutions, allow us to identify the different populations beyond any reasonable doubt. Moreover the individual GNR components exhibit the same absorbance spectral characteristics and corresponding retention times as the native GNR suspensions (Fig. 6). Thus,

single wavelength DAD detection at 520 nm, for this mixture, is sufficient to confirm the successful separation of the component GNRs. Our results also indicate there is no significant interparticle interaction between GNRs (which would result from chemical and/or physical interactions) in the mixed state or during the A4F measurements, respectively; such interactions would likely manifest themselves by the appearance of agglomerates.

Also, as all absorbance signals are identified for the different GNRs, it is possible to determine the selectivity; a very reasonable selectivity of 0.87 was obtained for this mixture. This indicates that the methodology developed in the present study has similar separation efficiencies for GNRs either as individual components or in complex mixtures.

It is well documented that for GNRs and gold nanoparticles alike, changes in the SPR bands can be observed upon changes in the aggregation state, and it was therefore necessary to check that no interaction occurred during the elution process that would alter the effective aspect ratio and size of the GNRs. Additionally, to support further confirmation of the identities of observed signals for the GNR mixture (see above), A4F measurements were conducted using a range of absorbance wavelengths. The resulting fractograms are represented in 3-dimensional (3D) format in Fig. 7. The fractograms collectively exhibit three peaks corresponding to the three GNR components. It appears that each peak position (along the retention time
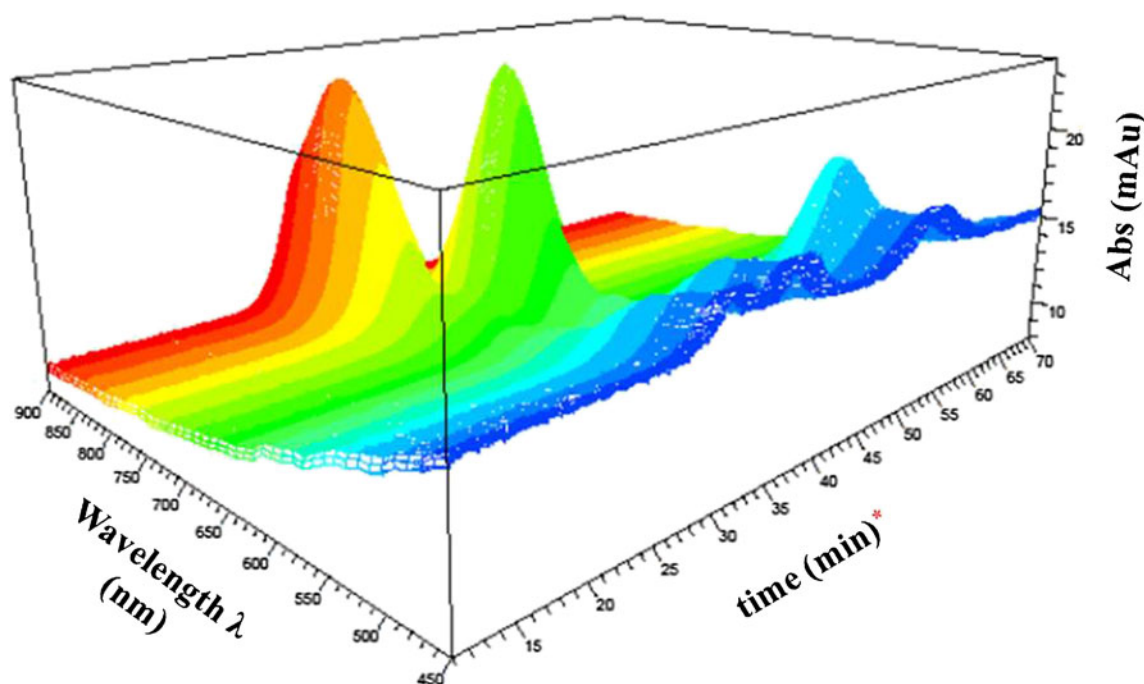

Fig. 7 3D representations of typical A4F fractogram (two different orientations) obtained for the GNR mixture using different optical absorbance wavelengths. Time represented here includes a focus and injection step of 11 min; therefore, to compare with previous reported elution times it is necessary to first subtract 11 min

axis) is constant, but the peak intensity changes depending on the wavelength observed. The peak located at lower retention time (t_R=19.8 min) has a higher intensity at 844 nm, which corresponds to the GNR4.4 longitudinal SPR band (λ_{max}=844 nm). A similar observation can be made for the second peak at a wavelength of 712 nm, which corresponds to GNR3.1 (λ_{max}=712 nm). Finally, for GNR1.4, with a longitudinal SPR band (λ_{max}=550 nm), the overlapping longitudinal (550 nm) and transverse (520 nm) bands correspond to the peak with the highest retention time. This result again demonstrates that the method allows separation of GNRs according to their aspect ratio. Additionally, in the 3D fractogram example (Fig. 7), no peaks were observed at wavelength positions that might indicate the presence of other morphologies resulting from the interaction of GNRs during focusing and elution.

It is worthwhile comparing characterization of the GNR mixture by A4F-DAD with that obtained in batch mode (i.e., "one pot analysis") using an off-line UV–vis spectrometer; even if the batch mode spectrum yields evidence of multiple GNR components present in the sample, it does not permit discrimination between different populations (especially for GNRs with a small aspect ratio). The lowest GNR aspect ratio (slightly above unity) has a longitudinal SPR band around 550 nm, close to and overlapping with the transverse mode at 520 nm common to all GNRs. So, here it is possible using the A4F-DAD method to separate and characterize GNRs with aspect ratios ranging from very small (close to spherical) to much higher values (more rod-like).

Conclusions

In this work, a novel application of A4F was demonstrated for the characterization of CTAB-stabilized GNRs based on their aspect ratio. We showed the capacity for A4F to fractionate positively charged nanoparticles (with pH in the range 3 to 4). The problem of irreversible adsorption of positively charged nanoparticles onto the A4F accumulation wall (negatively charged membrane) can be eliminated by controlling the mobile phase composition (e.g., the ratio between ammonium nitrate and CTAB, and ionic strength). The optimized condition affords a convenient retention time associated with the highest possible recovery. We then described and validated an A4F methodology that permits eluting GNRs according to their shape (i.e., aspect ratio). We believe this to be the first reported experimental study to clearly show the steric-entropic contribution of nanoparticle shape to the elution process by FFF, where the GNR diffusion coefficient, aspect ratio and orientation vector controls elution in normal mode A4F. This result, in accordance with FFF theory, is different from those obtained

in previous studies of nanowires and carbon nanotubes reported in the literature, where particles with the lowest aspect ratio eluted before the higher aspect ratio particles [18, 37]. Finally, we applied the developed methodology to fractionate GNR components within a complex mixture containing different aspect ratios. The results show that multi-wavelength optical absorbance detection can be relevant to interpret the shape of GNRs according to their retention time in A4F. The combination of absorbance detection with A4F has the advantage of in situ analysis (compared to, e.g., electron microscopy) to investigate GNR shape (aspect ratio) and to separate individual populations.

Further studies are required to evaluate the application of this method to characterize more complex mixtures of GNRs and other asymmetric nanoscale objects, and under a wider range of dispersion conditions. Additionally, we will expand this work to investigate tubular geometries with aspect ratios similar to the rod-like geometry studied here, and to demonstrate the broader applicability of the aspect ratio dependent elution behavior described in this work.

References

1. Beckett R, Giddings JC (1997) Entropic contribution to the retention of nonspherical particles in field-flow fractionation. J Colloid Interface Sci 186(1):53–59
2. El-Sayed MA (2001) Some interesting properties of metals confined in time and nanometer space of different shapes. Acc Chem Res 34(4):257–264
3. Murphy CJ, Sau TK, Gole AM, Orendorff CJ, Gao J, Gou L, Hunyadi SE, Li T (2005) Anisotropic metal nanoparticles: synthesis, assembly, and optical applications. J Phys Chem B 109 (29):13857–13870
4. Gormley AJ, Malugin A, Ray A, Robinson R, Ghandehari H (2011) Biological evaluation of RGDfK-gold nanorod conjugates for prostate cancer treatment. J Drug Target 19(10):915–924
5. Alekseeva AV, Bogatyrev VA, Dykman LA, Khlebtsov BN, Trachuk LA, Melnikov AG, Khlebtsov NG (2005) Preparation and optical scattering characterization of gold nanorods and their application to a dot-immunogold assay. Appl Opt 44(29):6285–6295
6. Singh R, Nalwa HS (2011) Medical applications of nanoparticles in biological imaging, cell labeling, antimicrobial agents, and anticancer nanodrugs. J Biomed Nanotechnol 7(4):489–503
7. Niidome T, Yamagata M, Okamoto Y, Akiyama Y, Takahashi H, Kawano T, Katayama Y, Niidome Y (2006) PEG-modified gold nanorods with a stealth character for in vivo applications. J Control Release 114(3):343–347
8. Huang X, Neretina S, El-Sayed MA (2009) Gold nanorods: from synthesis and properties to biological and biomedical applications. Adv Mater 21(48):4880–4910
9. Huang X, Jain PK, El-Sayed IH, El-Sayed MA (2007) Gold nanoparticles: interesting optical properties and recent applications in cancer diagnostics and therapy. Nanomedicine 2(5):681–693
10. Zhu Y, Kuang H, Xu L, Ma W, Peng C, Hua Y, Wang L, Xu C (2012) Gold nanorod assembly based approach to toxin detection by SERS. J Mater Chem 22(6):2387–2391

11. Xu L, Kuang H, Wang L, Xu C (2011) Gold nanorod ensembles as artificial molecules for applications in sensors. J Mater Chem 21 (42):16759–16782

12. Sekhon JS, Verma SS (2011) Optimal dimensions of gold nanorod for plasmonic nanosensors. Plasmonics 6(1):163–169

13. Pissuwan D, Valenzuela SM, Cortie MB (2008) Prospects for gold nanorod particles in diagnostic and therapeutic applications. Biotechnol Genet Eng Rev 25:93–112

14. Liu J-M, Wang H-F, Yan X-P (2011) A gold nanorod based colorimetric probe for the rapid and selective detection of Cu 2+ ions. Analyst 136(19):3904–3910

15. Narayanan R, El-Sayed MA (2007) Catalysis by metallic nanoparticles: the good and the bad. Chim Oggi 25(1):84–86

16. Wei G-T (1999) Shape separation of nanometer gold particles by size-exclusion chromatography. Anal Chem 71(11):2085–2091

17. Gigault J, Le Hécho I, Dubascoux S, Potin-Gautier M, Lespes G (2010) Single walled carbon nanotube length determination by asymmetrical-flow field-flow fractionation hyphenated to multi-angle laser-light scattering. J Chromatogr A 1217(50):7891–7897

18. Gigault J, Grassl B, Lespes G (2011) Multi-wall carbon nanotube aqueous dispersion monitoring by using A4F-UV-MALS. Anal Bioanal Chem 401(10):3345–3353

19. Cho TJ, Hackley VA (2010) Fractionation and characterization of gold nanoparticles in aqueous solution: asymmetric-flow field flow fractionation with MALS, DLS, and UV–vis detection. Anal Bioanal Chem 398(5):2003–2018

20. Calzolai L, Gilliland D, Garcìa CP, Rossi F (2011) Separation and characterization of gold nanoparticle mixtures by flow-field-flow fractionation. J Chromatogr A 1218(27):4234–4239

21. Bolea E, Jiménez-Lamana J, Laborda F, Castillo JR (2011) Size characterization and quantification of silver nanoparticles by asymmetric flow field-flow fractionation coupled to inductively coupled plasma mass spectrometry. Anal Bioanal Chem 401(9):2723–2732

22. Hagendorfer H, Kaegi R, Traber J, Mertens SF, Scherrers R, Ludwig C, Ulrich A (2011) Application of an asymmetric flow field flow fractionation multi-detector approach for metallic engineered nanoparticle characterization—prospects and limitations demonstrated on Au nanoparticles. Anal Chim Acta 706(2): 367–378

23. Kammer FVD, Baborowski M, Friese K (2005) Field-flow fractionation coupled to multi-angle laser light scattering detectors: applicability and analytical benefits for the analysis of environmental colloids. Anal Chim Acta 552(1–2):166–174

24. Phelan Jr FR, Bauer BJ (2008) Separation mechanisms for nanoscale spheres and rods in field-flow fractionation. Technical Proceedings of the 2008 NSTI Nanotechnology Conference and Trade Show, NSTI-Nanotech, Nanotechnology 2008. pp 179–182

25. Schmidt B, Loeschner K, Hadrup N, Mortensen A, Sloth JJ, Bender Koch C, Larsen EH (2011) Quantitative characterization of gold nanoparticles by field-flow fractionation coupled online with light scattering detection and inductively coupled plasma mass spectrometry. Anal Chem 83(7):2461–2468

26. Zattoni A, Rambaldi DC, Reschiglian P, Melucci M, Krol S, Garcia AMC, Sanz-Medel A, Roessner D, Johann C (2009) Asymmetrical flow field-flow fractionation with multi-angle light scattering detection for the analysis of structured nanoparticles. J Chromatogr A 1216(52):9106–9112

27. Jain PK, Eustis S, El-Sayed MA (2006) Plasmon coupling in nanorod assemblies: optical absorption, discrete dipole approximation simulation, and exciton-coupling model. J Phys Chem B 110(37):18243–18253

28. Link S, El-Sayed MA (1999) Spectral properties and relaxation dynamics of surface plasmon electronic oscillations in gold and silver nanodots and nanorods. J Phys Chem B 103(40):8410–8426

29. Smitha SL, Gopchandran KG, Ravindran TR, Prasad VS (2011) Gold nanorods with finely tunable longitudinal surface plasmon resonance as SERS substrates. Nanotechnology 22(26):265705

30. Guo H, Ruan F, Lu L, Hu J, Pan J, Yang Z, Ren B (2009) Correlating the shape, surface plasmon resonance, and surface-enhanced raman scattering of gold nanorods. J Phys Chem C 113(24):10459–10464

31. Kelly KL, Coronado E, Zhao LL, Schatz GC (2003) The optical properties of metal nanoparticles: the influence of size, shape, and dielectric environment. J Phys Chem B 107(3):668–677

32. Schimpf ME, Caldwell K, Giddings JC (2000) Field flow fractionation handbook. Wiley-IEEE

33. Garcia de la Torre JG, Bloomfield VA (1981) Hydrodynamic properties of complex, rigid, biological macromolecules: theory and applications. Q Rev Biophys 14(1):81–139

34. van der Zande BMI, Dhont JKG, Böhmer MR, Philipse AP (1999) Colloidal dispersions of gold rods characterized by dynamic light scattering and electrophoresis. Langmuir 16(2):459–464

35. Chun J, Fagan JA, Hobbie EK, Bauer BJ (2008) Size separation of single-wall carbon nanotubes by flow-field flow fractionation. Anal Chem 80(7):2514–2523

36. Chen B, Selegue JP (2002) Separation and characterization of single-walled and multiwalled carbon nanotubes by using flow field-flow fractionation. Anal Chem 74(18):4774–4780

37. Phelan Jr FR, Bauer BJ (2007) Simulation of nanotube separation in field-flow fractionation (FFF). Chem Eng Sci 62(17):4620–4635